FDTD Voxels-in-Cell Method With Debye Media

Kenan Tekbaş, *Member, IEEE*, Jean-Pierre Bérenger, *Fellow, IEEE*,
Luis Manuel Diaz Angulo, *Member, IEEE*, Miguel Ruiz-Cabello,
and Salvador G. Garcia, *Senior Member, IEEE*

Abstract— The Voxels-in-Cell (VIC) method was recently introduced to reduce the computational cost of the finite-difference time-domain (FDTD) method with objects composed of dielectric voxels. It relies on using an FDTD cell larger than the voxels, with eight or more voxels in each VIC cell. With the objective of using it in bio-electromagnetics applications, this article extends the VIC method to voxels filled with Debye media. Besides the theory and the algorithm of the extended VIC method, several numerical experiments are reported with a canonical object and with human body phantoms composed of voxels. The experiments show that the accuracy of the method is preserved while large reductions of the computational requirements can be achieved, especially the computational time can be reduced by about one order of magnitude.

Index Terms— Bio-electromagnetics, Debye media, finite-difference time-domain (FDTD), phantom, voxels.

I. Introduction

THE Voxels-in-Cell (VIC) method was introduced in [1] with the objective of reducing the computational cost of finite-difference time-domain (FDTD) simulations when the object of interest is given as a set of voxels. The idea behind the method consists of using an FDTD cell larger than the voxels, with for instance eight voxels in each cell. The framework of the VIC method [1] is summarized in Fig. 1. As compared to using cells equal in size to the voxel size, the overall number of cells is widely reduced while the FDTD time step can be enlarged, resulting in a large reduction of the computational burden.

Initially presented with pure dielectric objects [1], the VIC method is now extended to dispersive Debye media. This allows the method to be used in bio-electromagnetics, where the human phantoms are composed of voxels assumed as
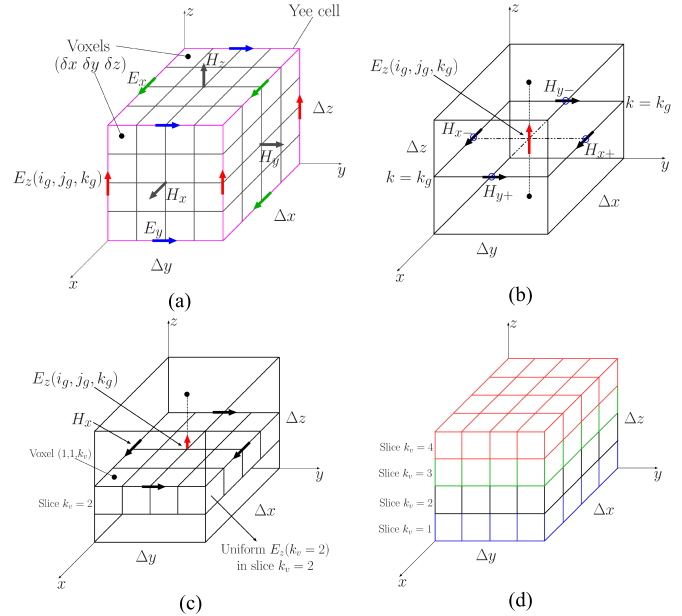
Fig. 1. Summary of the VIC method, as with dielectric media in [1]. With Debye media, in addition to the E-field computed in the slices and the H-field in the cells, the electric flux density D is computed in each voxel. (a) Yee cell as usually defined, with E nodes on its edges, is filled with voxels. (b) Yee cell shifted with $\Delta x/2$ and $\Delta y/2$ with respect to (a), with the E_z node at its center, denoted as $E_z(i_g, j_g, k_g)$. (c) E_z-field in each slice, denoted as $E_z(k_v)$, is uniform, but discontinuous at the interfaces between slices, thus it is updated in each slice using the Maxwell-Ampere law that yields (12) in Debye media. From which D_z in each voxel of the slices is updated using (10). (d) $E_z(i_g, j_g, k_g)$ at the center of the cell in (b) or (c), to be used later for updating the neighboring H components, is updated using (13) and $E_z(k_v)$ in the slices. Note that there is no need of computing D_z at the $E_z(i_g, j_g, k_g)$ node. The other electric field components, E_x and E_y, are treated using the same logic.

Debye media [2]. Such an achievement was not possible with methods [3], [4], [5], [6], since they are limited to a single interface splitting the FDTD cell into two parts, one filled with vacuum or dielectric, the other with a dispersive medium. Inversely, the VIC method can handle the several non-parallel interfaces present in the FDTD cells when they are filled with voxels.

The modifications of the theory for dealing with Debye media are described and experiments are reported with a canonical object and with the head of a human phantom, in both cases with VIC cells two times larger than the voxels (eight voxels in each VIC cell). The experiments show that the accuracy of the method is roughly similar to that with dielectric media [1]. A critical issue is addressed, namely the reduction of the computational requirements by using the VIC method in place of a fine grid with a cell size equal to the voxel

size. It is shown that reductions of the computational time of one order of magnitude can be achieved. Finally, simulations with two whole human phantoms illustrate what can be done with the VIC method using a personal computer (PC).

II. DERIVATION OF FDTD UPDATE EQUATIONS

A. Homogeneous FDTD Cell

Let us assume that the electric flux density D_z is centered in the cell of sizes Δx, Δy, Δz (same arrangement as in Fig. 1(b), with D_z in place of E_z). The magnetic field nodes H_{y-} and H_{y+} are situated $\Delta x/2$ from D_z, whereas the nodes H_{x-} and H_{x+} are $\Delta y/2$ away from D_z. With the FDTD method, these components are used to update D_z by discretizing the integral form of the Maxwell-Ampere equation

$$\iint_{\Delta x \Delta y} \frac{\partial D_z(t)}{\partial t} dx dy = C_h(t) \tag{1}$$

where t is the time, $\Delta x \ \Delta y$ is the surface perpendicular to D_z and C_h is the integral

$$C_h(t) = \int_L H(t) dl \tag{2}$$

where L is the contour path that surrounds surface $\Delta x \ \Delta y$ and holds the four H nodes. Discretization of $C_h(t)$ at time $n+1/2$ reads

$$C_h^{n+1/2} = \left(H_{y+}^{n+1/2} - H_{y-}^{n+1/2} \right) \Delta y - \left(H_{x+}^{n+\frac{1}{2}} - H_{x-}^{n+\frac{1}{2}} \right) \Delta x. \tag{3}$$

Assuming that the flux D_z is homogeneous in the cell, discretizing the derivative on time in (1) yields

$$\Delta D_z^{n+1/2} = \frac{\Delta t}{\Delta x \Delta y} C_h^{n+1/2} \tag{4}$$

where $\Delta D_z^{n+1/2}$ is the difference between D_z values at times n and $n+1$

$$\Delta D_z^{n+1/2} = D_z^{n+1} - D_z^n. \tag{5}$$

The electric flux D_z and field E_z share the same FDTD nodes and the relationship that connects them for the one-pole Debye model reads

$$D_z = \varepsilon_0 \left[\varepsilon_\infty + \frac{\varepsilon_S - \varepsilon_\infty}{1 + j\omega\tau} + \frac{\sigma}{j\omega\varepsilon_0} \right] E_z \tag{6}$$

where ε_∞ is the optical permittivity, ε_S is the static permittivity, ε_0 is the vacuum permittivity, σ is the static conductivity, τ is the relaxation time, and ω is the angular frequency. Component E_z at time $n+1$ from (6) can be obtained in the function of E_z and ΔD_z at previous time steps by using the discretized auxiliary equation similar to (see [7, eq. (16)]). Using (5), flux D_z can be eliminated from the auxiliary equation that becomes

$$E_z^{n+1} = \alpha_1^{-1} \left(\alpha_2 E_z^n - \alpha_3 E_z^{n-1} + \Delta D_z^{n+1/2} - \beta \Delta D_z^{n-1/2} \right) \tag{7}$$

where

$$\alpha_1 = A + B + 0.5C, \quad \alpha_2 = 2A + B - 0.5C, \quad \alpha_3 = A, \quad \beta = \tau/S$$

and

$$A = \varepsilon_0 \varepsilon_\infty \tau/S, \quad B = (\varepsilon_0 \varepsilon_S + \sigma\tau)\Delta t/S, \quad C = \sigma(\Delta t)^2/S,$$
$$S = \tau + \Delta t.$$

We note that we have replaced the update of flux D_z with the update of its increment ΔD_z over the time step, inversely to what is done in [7]. This permits the needed storage to be reduced, only ΔD_z at one time step instead of D_z at two time steps. In addition, the algorithm is slightly more rapid. In human body applications, in general flux D_z is not needed, in case it is needed at some nodes, it can be obtained from ΔD_z. The same substitution of D_z with ΔD_z is used in the following with non-homogeneous cells which also reduces the needed memory.

B. Non-Homogeneous FDTD Cell

Let us now address the case in Fig. 1 where the cell is non-homogeneous and split into $M_i M_j M_k$ voxels, each with its own medium and indexes (i_v, j_v, k_v), where $i_v \in (1, \underline{M}_i)$, $j_v \in (1, \underline{M}_j)$, $k_v \in (1, \underline{M}_k)$. In a given slice, the component E_z is tangential to the interfaces between the voxels of the slice, and thus it is continuous through those interfaces. Since the cell size in FDTD is small compared to the wavelength, we can assume that E_z is uniform in the slice, i.e., it is the same in all the voxels of the slice. Inversely, D_z is not continuous at the interfaces, so each voxel of the slice has its own D_z. The Maxwell-Ampere (1) law holds everywhere in the physical medium, including the slices composed of voxels. This allows us to derive the FDTD update of E_z and D_z as with a homogeneous cell, with only slightly more complicated mathematics, but without any further assumption on the Physics. For slice k_v, (1) yields the discrete integral at time t

$$\sum_{i_v=1}^{M_i} \sum_{j_v=1}^{M_j} \frac{\partial D_z(i_v, j_v, k_v, t)}{\partial t} \delta x \delta y = C_h(t) \tag{8}$$

that can be discretized as

$$\sum_{i_v=1}^{M_i} \sum_{j_v=1}^{M_j} \Delta D_z^{n+1/2}(i_v, j_v, k_v) \delta x \delta y = \Delta t C_h^{n+1/2} \tag{9}$$

where $\Delta D_z^{n+1/2}(i_v, j_v, k_v)$ is the increment of $D_z(i_v, j_v, k_v)$ in each voxel, similar to (5). In each voxel, the same auxiliary equation (7) as in a homogeneous cell holds, which provides us with $M_i M_j$ equations that can be rewritten as

$$\Delta D_z^{n+1/2}(i_v, j_v, k_v)$$
$$= \alpha_{1,i_v,j_v,k_v} E_z^{n+1}(k_v) - \alpha_{2,i_v,j_v,k_v} E_z^n(k_v)$$
$$+ \alpha_{3,i_v,j_v,k_v} E_z^{n-1}(k_v) + \beta_{i_v,j_v,k_v} \Delta D_z^{n-1/2}(i_v, j_v, k_v) \tag{10}$$

where coefficients α_{m,i_v,j_v,k_v} and β_{i_v,j_v,k_v} depend on the physical parameters in the voxel (i_v, j_v, k_v). Equations (9) and (10) form a set of $M_i M_j + 1$ equations in slice k_v for the unknown $E_z^{n+1}(k_v)$ and the $M_i M_j$ unknowns $\Delta D_z^{n+1/2}(i_v, j_v, k_v)$. The set can be easily solved as the set of three equations in (see [7, eq. (17)]) by using the $M_i M_j$ equations (10), so as to

replace the $M_i \, M_j$ unknowns $\Delta D_z^{n+1/2}(i_v, j_v, k_v)$ in (9). This yields

$$
\begin{aligned}
\sum_{i_v=1}^{M_i} \sum_{j_v=1}^{M_j} & \left[\alpha_{1,i_v,j_v,k_v} E_z^{n+1}(k_v) - \alpha_{2,i_v,j_v,k_v} E_z^n(k_v) \right. \\
& \left. + \alpha_{3,i_v,j_v,k_v} E_z^{n-1}(k_v) + \beta_{i_v,j_v,k_v} \Delta D_z^{n-1/2}(i_v, j_v, k_v) \right] \\
& = \frac{M_i M_j \Delta t}{\Delta x \Delta y} C_h^{n+1/2}.
\end{aligned}
\tag{11}
$$

The sole unknown in (11), $E_z^{n+1}(k_v)$, can then be obtained as

$$
\begin{aligned}
E_z^{n+1}(k_v) = c_1(k_v)^{-1} & \left[\frac{M_i M_j \Delta t}{\Delta x \Delta y} C_h^{n+1/2} + c_2(k_v) E_z^n(k_v) \right. \\
& \left. - c_3(k_v) E_z^{n-1}(k_v) - \vartheta(k_v) \right]
\end{aligned}
\tag{12}
$$

with $C_h^{n+1/2}$ from (3) and

$$
c_1(k_v) = \sum_{i_v=1}^{M_i} \sum_{j_v=1}^{M_j} \alpha_{1,i_v,j_v,k_v}, \quad c_2(k_v) = \sum_{i_v=1}^{M_i} \sum_{j_v=1}^{M_j} \alpha_{2,i_v,j_v,k_v}
$$

$$
c_3(k_v) = \sum_{i_v=1}^{M_i} \sum_{j_v=1}^{M_j} \alpha_{3,i_v,j_v,k_v}
$$

$$
\vartheta(k_v) = \sum_{i_v=1}^{M_i} \sum_{j_v=1}^{M_j} \left[\beta_{i_v,j_v,k_v} \Delta D_z^{n-1/2}(i_v, j_v, k_v) \right].
$$

Once $E_z^{n+1}(k_v)$ has been computed, the $M_i M_j$ unknowns $\Delta D_z^{n+1/2}(i_v, j_v, k_v)$ can be obtained by using the auxiliary equation (10) that holds in each voxel.

After updating $E_z(k_v)$ and its x and y counterparts in all the slices of all the FDTD cells, the H components should be updated to complete the FDTD iteration. This can be done as with dielectric voxels in [1]. The standard FDTD algorithm can be left unchanged, we just need to place the average value $< E_z^{n+1} >$ over Δz at each original $E_z(i_g, j_g, k_g)$ node of the FDTD cells, that is,

$$
E_z^{n+1}(i_g, j_g, k_g) = \frac{1}{M_k} \sum_{k_v=1}^{M_k} E_z^{n+1}(k_v).
\tag{13}
$$

Finally, with cells filled with voxels, the FDTD advance of E_z and ΔD_z components can be summarized as follows:
1) Compute $E_z^{n+1}(k_v)$ in each slice using (12).
2) Compute $\Delta D_z^{n+1}(i_v, j_v, k_v)$ in each voxel using (10).
3) Compute the average of $E_z^{n+1}(k_v)$ in the cell (13), to be used later for the advance of H components with the standard FDTD equation.

It can be shown that the above VIC method reduces to the previously presented method [8] in the special case of transverse-magnetic (TM) polarization in 2-D problems.

III. Methods With Which VIC Is Compared

The VIC calculations are compared with similar calculations as in [1].

1) A reference calculation using an FDTD fine grid, where the cell size is identical to the voxel size δx, δy, δz, with each cell filled with one voxel. The E nodes are located on the edges

of the fine cells, which are also the edges of the voxels, and the updates of the E components comply with the Maxwell-Ampere law. With dielectric media [1], this just consists of averaging the permittivity in the four voxels surrounding the considered E node. With Debye media, the E-field remains the same in the volume of the cell where the E node is centered because it is continuous at the interfaces, but the D-fields are different in the four media of that volume composed of four quarters of voxels. The problem is the same as in a slice of the VIC cells. This means that we can get one equation like (9) and four equations like (10). From which E can be updated with an equation like (12) and then ΔD_z with four equations like (10). This solution is rigorous. A simpler implementation of Debye voxels has been sometimes used with FDTD, it consists of shifting by half a cell the voxels in two directions, so the E-field to be updated is at the center of one voxel. Then, (4) and (7) can be applied. However, the shifts depend on the component, due to the FDTD staggered grid, which means that the medium is not rigorously the same for the three E components. This method is only an approximation. We performed some comparisons of the two methods. A significant difference was observed at some nodes, in the proximity of high contrast at interfaces or corners. In this article, all the reported fine grid results were computed with the rigorous method.

2) A calculation denoted as AVG, using a coarse cell that has the same sizes and location as the VIC cell. The medium parameters used to update E equal the average values in the volume with dimensions of Δx, Δy, Δz and whose center is located at the E node. This reads, for component $E_z(i_g, j_g, k_g)$ in Fig. 1

$$
\chi(i_g, j_g, k_g) = \frac{\sum_{i_v=1}^{M_i} \sum_{j_v=1}^{M_j} \sum_{k_v=1}^{M_k} \chi(i_v, j_v, k_v)}{M_i M_j M_k}
\tag{14}
$$

where χ is either ε_∞, ε_S, σ, or τ. The medium is thus assumed as homogeneous in the AVG cell so that both E and D can be updated using (4) and (7).

IV. Experiments With a Complex Canonical Object

In this section, we report experiments with the $60 \times 60 \times 60$ VIC cell canonical object mimicking the topology of the human body. Here, the three dielectric media in [1] are replaced with three human body media, skin, fat, and bone. The parameters of the media are shown in Fig. 2. The computational settings are the same as in [1], i.e., voxel size 1 mm^3, VIC cell size (2 mm)^3, VIC time step 3.66 ps, the object surrounded with a vacuum and a PML, and the incident plane wave propagating in y direction and polarized in the z-direction, with waveform

$$
E_z(t) = 100 \exp\left[-((t - 3\mathcal{T})/\mathcal{T})^2 \right] \text{V/m}
\tag{15}
$$

where $\mathcal{T} = 134.5$ ps.

The situations of the corners of the object are defined as in [1] where they are represented and numbered in the 2-D case in [1, Fig. 6] and numbered in the 3-D case in [1, Fig. 16]. In 3-D the corner represented in [1, Fig. 16], in gray, is the
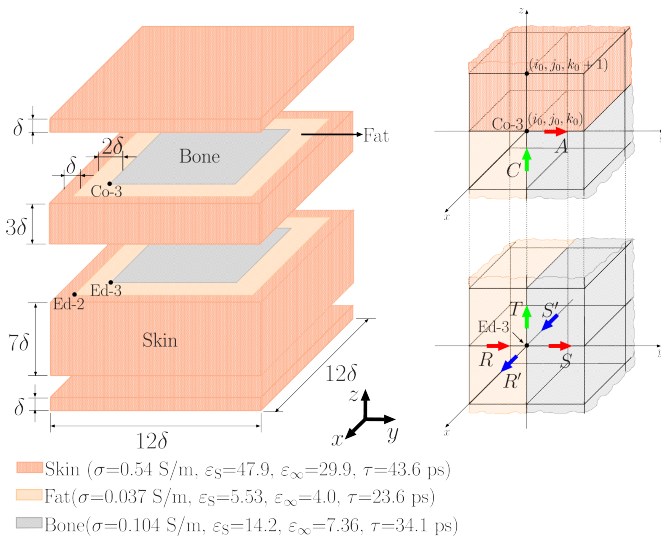
Fig. 2. Object mimicking the human body with three Debye media. $\delta = 5$ VIC cells. Points denoted as Co-3, Ed-2, and Ed-3, are locations of corners and edges, respectively, where E-fields are plotted in Figs. 3 and 4. There are eight different situations of the object with respect to the VIC grid, as with the same object in [1], and more generally, as with any object when there are eight voxels in the VIC cell, e.g., situation 1 with the Co-3 at (i_0, j_0, k_0) in (see [1, Fig. 16]), situation 2 at $(i_0-1/2, j_0, k_0)$, situation 3 at $(i_0, j_0+1/2, k_0)$, situation 4 at $(i_0-1/2, j_0+1/2, k_0)$, situation 5 at $(i_0, j_0, k_0+1/2)$, situation 6 at $(i_0-1/2, j_0, k_0+1/2)$, situation 7 at $(i_0, j_0+1/2, k_0+1/2)$, and situation 8 at $(i_0-1/2, j_0+1/2, k_0+1/2)$. The electric fields were recorded at nodes A and C of Co-3, and at nodes R, R', S, S', and T of Ed-2 and Ed-3.

situation 1, while for instance, situation 3 in 3-D corresponds to a corner situated at $(i_0-1/2, j_0 + 1/2, k_0)$, i.e., shifted to the right with $\Delta y/2$ with respect with the corner in situation 1. Fig. 3 reports the E_y and E_z fields at the inner corner denoted as Co-3 (see Fig. 2) which is a point the three media have in common, while Fig. 4 shows E-fields at the inner edge Ed-2 between skin and fat and Ed-3 between fat and bone. The exact locations A, C, R, S, R', S', T of the plotted E are the same as in (see [1, Figs. 16 and 22]). The same situations of the object are plotted, so that we can compare Figs. 3 and 4 with [1, Figs. 27 and 28].

Results in Fig. 3 are roughly similar to the ones in (see [1, Fig. 27]). However, the magnitude of the fields, especially the peak values, are lower with the Debye media than with the pure dielectric media. The oscillations of the fields are significantly reduced, which is due to the presence of loss terms with the Debye media, while the pure dielectric media are lossless. Similar reductions of the magnitudes are observed in the vicinity of the edges (see Fig. 4), but with little reduction of the oscillations of the fields.

Concerning the difference between the VIC results and the fine grid results, i.e., the VIC error, in Figs. 3 and 4 it is quite small as in the pure dielectric cases (see [1, Figs. 27 and 28]). Especially, the VIC component tangential to the edge, which is not singular (node T in Fig. 4), is superimposed to the fine grid component, as with pure dielectric media.

The observations on Figs. 3 and 4 are general. At any outputted node the agreement of VIC with fine grid calculation is similar to that observed with pure dielectric media, in both cases there is a significant difference only for the components that are singular at corners or edges. The magnitude of the field
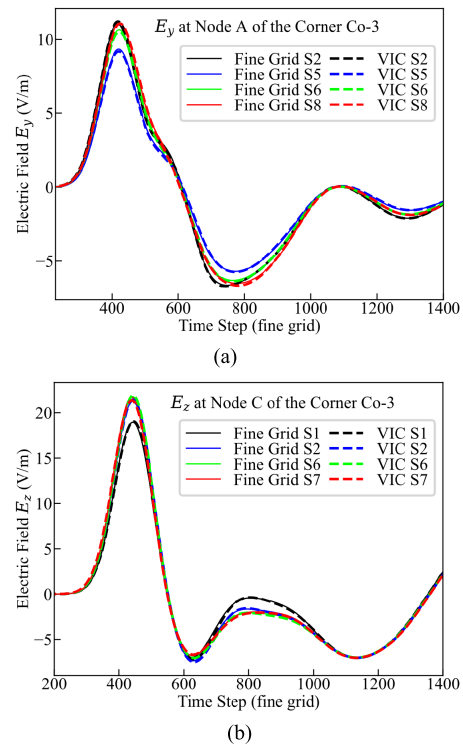

Fig. 3. Results at the corner Co-3. Comparison of fine grid E with VIC E (a) at node A and (b) at node C. The errors in both cases are so small in all the situations that any situation can be considered almost exact.
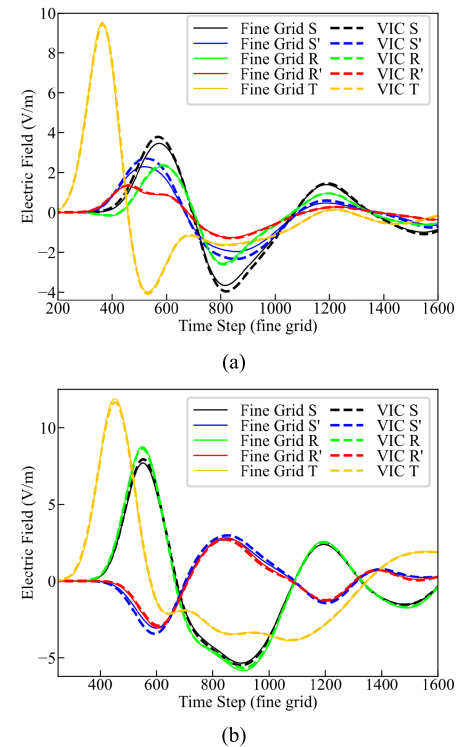

Fig. 4. Results with situation 4 (a) at edge Ed-2, where node T results are multiplied with 0.25 and (b) at edge Ed-3, where node T results are multiplied with 0.5.

within the object depends on the situation of the observation. From the outer surface of the object to its interior, the field
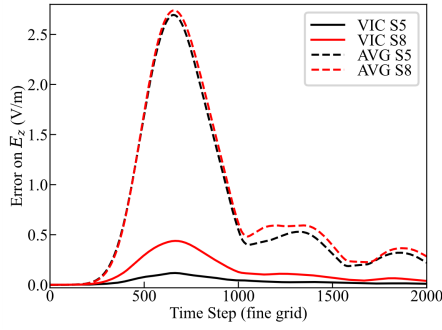
Fig. 5. Overall average error of the electric field E_z in situations 5 and 8 of the object (the largest errors of VIC). It includes all nodes in the object and three VIC cells of its surrounding vacuum.
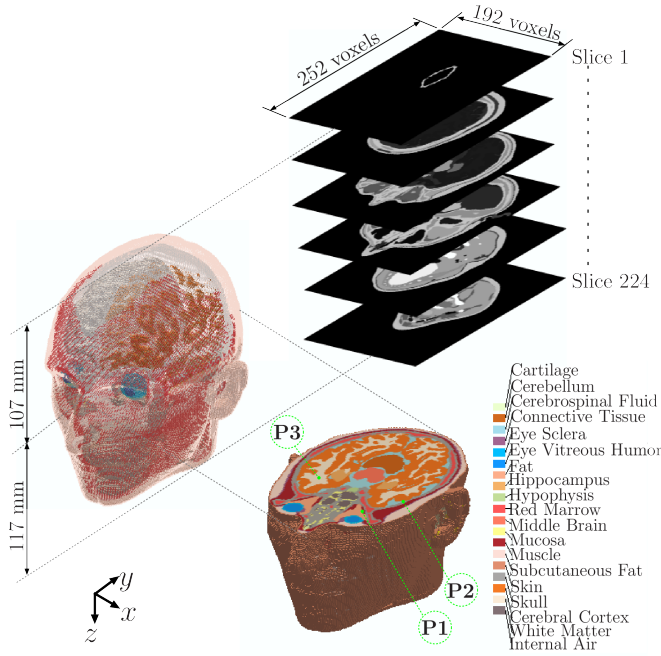

Fig. 6. Three-dimensional human head model was imported from the human phantom [9] in the form of 224 slices of 192×252 voxels. Each tissue was associated with its own one-pole Debye parameters [10]. The observation points P1, P2, and P3 were located behind the left eyeball, in the cranial portion of the skull, and in the white matter, respectively.

decreases faster than in the pure dielectric case, because of the propagation in the lossy Debye media.

Fig. 5 reports the average of the VIC and AVG errors on the $60 \times 60 \times 60$ cell object surrounded with a layer of vacuum three cells in thickness, computed as in [1]. Comparing Fig. 5 with (see [1, Fig. 30]), the errors are quite similar at an early time, but at a late time, the errors in Fig. 5 are significantly smaller because of the losses in the human body media.

V. SIMULATIONS WITH A HUMAN PHANTOM HEAD

We performed simulations with the head of the Voxel-Phantom provided by IT'IS Foundation (Zurich, Switzerland) [9]. The voxel size is 1 mm³. The simulation scenario is depicted in Fig. 6. In both the fine grid and the VIC grid, we imported a part of the Phantom composed of $192 \times 252 \times 224$ voxels that can be viewed as composed with 224 slices perpendicular to direction z and one voxel in thickness (see

Fig. 6). Each slice has 192×252 voxels in (x, y) directions. Note that the voxels of each slice are filled with either head media or vacuum. The fine grid was an FDTD domain of $240 \times 300 \times 272$ cells, surrounded by a 12 cell PML. The head (see Fig. 6) was imported in the center of the domain, which means that there were a 24 cell layer of vacuum between the slices in Fig. 6 and the PML. In the VIC grid, the cell was $(2 \text{ mm})^3$ in size. The imported head (see Fig. 6) was composed with VIC cells, each one with eight voxels inside, which means 96 VIC cells in the x-direction, 126 in the y-direction, and 112 in the z-direction. The VIC counterpart of the $192 \times 252 \times 224$ voxels or fine grid cells was thus a VIC grid of size $96 \times 126 \times 112$. It was surrounded with a layer of vacuum 12 cells in thickness, having the same physical thickness as the 24 cell layer of vacuum in the fine grid. For the convenience of encoding, the 12 cell layer of vacuum was the addition of a 2 cell VIC layer and a 10 cell layer of usual FDTD cells, in the manner of (see [1, Fig. 4]). A 12 cell PML was placed outside the vacuum. In total, the overall FDTD domains were $264 \times 324 \times 296$ for the fine grid calculation and $144 \times 174 \times 160$ for the VIC and AVG calculations. The Debye parameters for all human tissues in the phantom are presented in [10]. The incident plane wave and the FDTD steps were the same as in Section IV. Inversely to the previous experiments, we did not vary the situation of the phantom in the VIC grid, we considered only the situation resulting from the import of the $192 \times 252 \times 224$ voxel part of the phantom that just fits a $96 \times 126 \times 112$ VIC grid.

Fig. 7 reports the three field components at their nodes closest to points P1, P2, and P3 in Fig. 6. We can see that the VIC results agree very well with the reference fine grid solutions, at P1, P2, and P3. Inversely, the AVG results depart from the reference solutions at P1 and P2, especially at P1 where E_x and E_z are strongly erroneous.

The interpretation of the results is complex in such a strongly non-homogeneous structure, where errors propagating from neighboring nodes may be added to the local error. However, beside the excellent agreement of VIC results with the references, the discordance of AVG results in Fig. 7 seems in accordance with the situations of locations P1, P2, and P3. At P1, the eight voxels that surround the plotted E_z VIC node (see the situations of the components with respect to the voxels in [1, Fig. 15]) are filled with different media, some with fat, some with muscle, whereas the voxels that surround E_x and E_y are all filled with fat. From this, E_z is discontinuous in the volume composed with the eight voxels [1], which results in the large error of AVG in Fig. 7(a). At P2, this is E_y that is discontinuous, the surrounding voxels are filled either with skull or cerebrospinal fluid, whereas E_x and E_z VIC nodes are in homogeneous skull medium. The lower AVG errors in Fig. 7(b) are, at least in part, due to the lower contrast of the media at P2. At P1 the permittivity's of fat and muscle are about 5.5 and 57, respectively, while at P2 the permittivity's of skull and cerebrospinal Fluid are about 14 and 70. At P3, VIC, AVG, and fine grid results are almost superimposed. This is because P3 is in homogeneous region (white matter) from which no local error is produced by AVG which is equivalent to VIC.
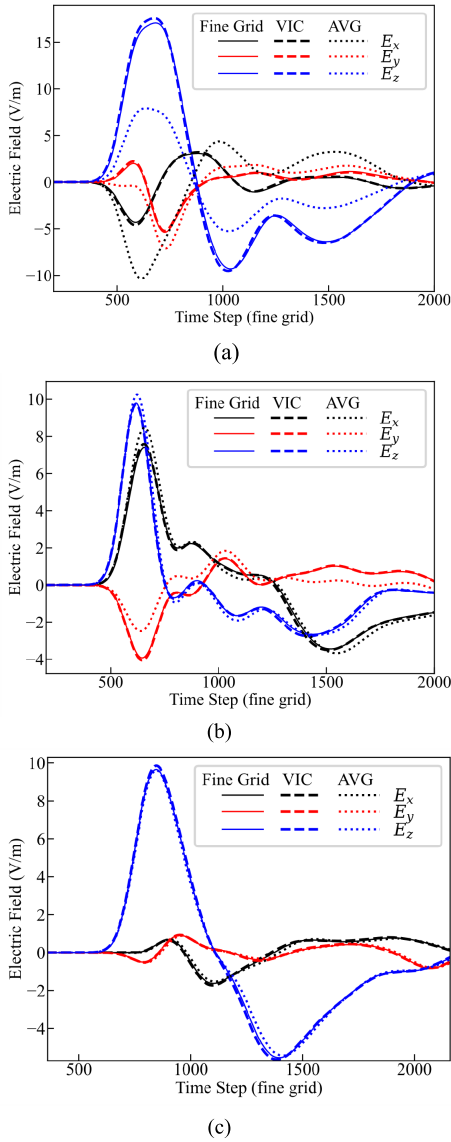
(a)

(b)

(c)

Fig. 7. Results with Fine Grid, VIC, and AVG methods (a) at P1, (b) at P2, and (c) at P3, within the head of the phantom.
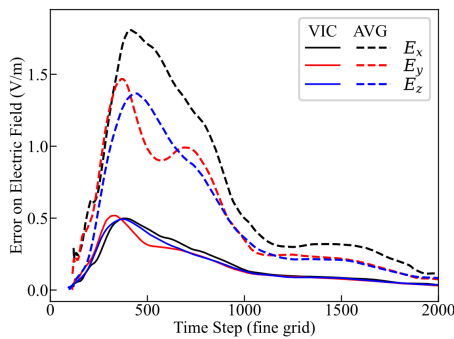

Fig. 8. Overall average error of the electric field components. It includes all the nodes within the head of the phantom and two VIC cells of its surrounding vacuum, but the nodes where $|E| < 1.0$ V/m were excluded.

Fig. 8 reports the average of the VIC and AVG errors on the phantom head surrounded with two VIC cells of vacuum, computed as in [1], except that the nodes where $|E|$ is lower than 1 V/m are excluded. The errors are smaller than with the

TABLE I
NUMBER OF HOMOGENEOUS AND NON-HOMOGENEOUS VIC-E CELLS IN THE PHANTOM HEAD

Nodes	Homogeneous cells (iflag=1)	Non-Homogeneous cells (brute force)
VIC-E_x	359066	226172
VIC-E_y	359292	226044
VIC-E_z	361089	222543

canonical object in Fig. 5 because 1/the object is larger so that the part of the object where the incident field is small is larger, and 2/the propagation of the field in the lossy Debye media is longer. The ratio of AVG error to VIC error is slightly smaller than in Fig. 5 which may be, at least in part, due to the lower contrast between media in the head which may reduce the AVG error. As in the dielectric case [1], the VIC method is stable, we have not found any instability with more than 5000 VIC time steps in all the simulations.

VI. OPTIMIZED ALGORITHMS FOR REDUCTION OF THE CPU TIME

With dielectric media and VIC cells two times larger than the voxels, the CPU time is in theory reduced with a factor of 16, as compared to a simulation using a cell equal in size to the voxels [1]. With Debye media, things are different, because of the more complex relationship between E and D vectors, which results in more complex updates. More specifically, E must be updated in each slice with (12), while D must be updated in each voxel with (10), which means ten update equations per cell. From this, there is no such simple theoretical reduction of CPU time as with dielectric media. Estimates of the ratio of CPU times by counting the number of operations suggest that the reduction of CPU times is lower than with dielectric media. This has been confirmed by experiments.

In the above as well as in [1], it is implicitly assumed that all the VIC cells surrounding components E_x, E_y, E_z, are non-homogeneous, i.e., as if all the eight voxels were different. Actually, this is not true in most applications, especially in bioelectromagnetics, where the phantoms are composed of homogenous organs, separated by interfaces. Therefore, parts of the VIC cells are homogeneous, with eight identical voxels, and the remaining VIC cells are non-homogeneous, usually with less than eight different voxels. As an example, in the phantom head in Fig. 6, approximately 60% of VIC cells in the head are homogeneous as indicated in Table I, where, for instance, VIC-E_x denotes the VIC cell having E_x at its center. This suggests that the CPU time could be reduced by using simplified updates in some VIC cells instead of the general updates (12) and (10), especially in the homogeneous ones where the update reduces to (4) and (7), which means two update equations instead of 10. We refer to the general case were all the eight voxels are different as the "brute force" update.

The reduction of CPU time can be achieved gradually by initially focusing on the update process for the simplest VIC cells. To begin with, assuming the brute force update is already
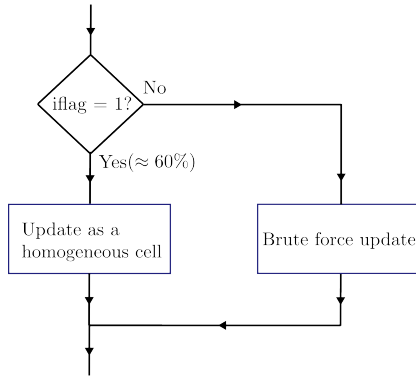
Fig. 9. Algorithm 1: simplified updates in the homogeneous VIC cells and brute force updates in the inhomogeneous ones, using just one "if" test.

Fig. 10. Algorithm 2: with treatment of VIC cells with at least one homogeneous slice.

implemented, the first step is to incorporate the treatment of homogeneous VIC cells. Assuming that each VIC cell, e.g., E_z VIC cell, has been provided with a flag before loop on time which equals 1 (iflag=1) if the VIC cell is homogeneous, then the block diagram of the update of the VIC cells would be as in Fig. 9. With just this simple addition of treatment of homogeneous cells, the CPU time for updating the Debye object will be widely reduced, since about 60% of the cells in the head will have iflag=1 and thus will be updated with (4) and (7). Concerning the VIC cells outside the Debye object and filled with vacuum, if any, as the ones in the slices of the imported head (see Fig. 6), they can be updated as usual FDTD cells in vacuum, so that one can consider that a branch with for instance iflag=0 could be added to the diagram in Fig. 9 to update these cells.

The next step in the optimization process involves addressing VIC cells that have at least one homogeneous slice. This comprises three cases: 1) the two slices are homogeneous but with different media; 2) slice 1 is homogeneous while slice 2 is non-homogeneous; and 3) the inverse case. Table II provides the number of non-homogeneous cells in the three cases, for the same head phantom as in Table I. We can introduce additional flags, before the time loop, corresponding to the three cases. Specifically, we assign "11" if both slices are homogeneous but with different media, "12" if the first slice is homogeneous and the second slice is non-homogeneous, and "21" if the first slice is non-homogeneous and the second slice is homogeneous. This optimization is visualized using a block diagram as Fig. 10, similar to Fig. 9.

Table II indicates that about 60% of the non-homogeneous cells in Table I belong to one of the three cases where at least one slice is homogeneous. This implies that in about 25% of all VIC cells, equation (12) and four equations (10) can be replaced with equations (4) and (7) in at least one slice. The remaining cells to be updated with brute force only represent about 17% of the total number of VIC cells (about 100 000 out of 580 000).

Table III reports the CPU times for 100 VIC iterations (11th Gen Intel[1] Core[2] i7-1165G7 @ 2.80 GHz), with the head phantom and brute force, algorithm 1, and algorithm
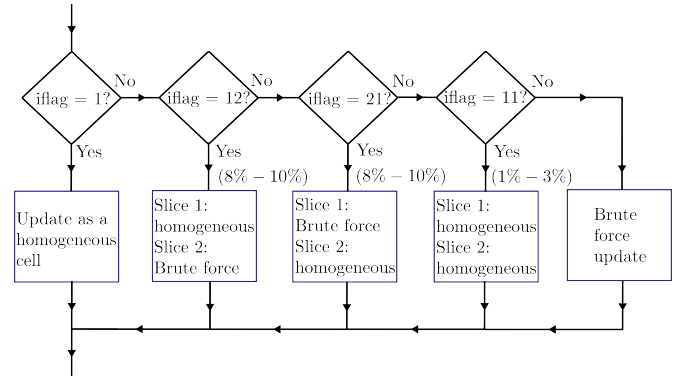
[1]Registered trademark.
[2]Trademarked.

TABLE II
NUMBER OF VIC-E CELLS HAVING AT LEAST ONE HOMOGENEOUS SLICE IN THE PHANTOM HEAD

Nodes	Both slices Homog. (iflag=11)	Homog. Slice 1 (iflag=12)	Homog. slice 2 (iflag=21)	Other (brute force)
VIC-E_x	18202	63396	63049	81552
VIC-E_y	8614	56183	56366	104881
VIC-E_z	11119	52276	52125	107023

TABLE III
CPU TIME (S) WITH VIC AND FINE GRID FOR THE PHANTOM HEAD

	VIC	rigorous fine grid	approximate fine grid
Brute force	11.9	102.6	62.5
Algorithm 1	8.6	81.3	N. A.
Algorithm 2	8.3	N. A.	N. A.

2 calculations, along with the CPU times for 200 iterations of the two fine grid calculations (see Section III). All the CPU times are the ones devoted to the Debye cells, excluding the surrounding cells of vacuum in Fig. 6. In the rigorous fine grid method, (12) and four equations (10) are employed for updating E and the four D's within the non-homogeneous cells, which occur when different media are present, while (4) and (7) are utilized in homogeneous cells. This is the same strategy as with VIC i.e., an algorithm like Algorithm 1 of VIC can be applied. With the approximate fine grid method, all the cells are homogeneous, and updates (4) and (7) are used everywhere.

One can see in Table III that even with the brute force VIC updates, the CPU time of VIC is widely smaller than with the rigorous fine grid updates (11.9 s instead of 102.6) or with the approximate fine grid (62.5 s). Algorithm 1 further reduces the CPU time significantly (8.6 s), but Algorithm 2 achieves little additional reduction (8.3 s). Table IV presents the reduction factors of CPU times deduced from Table III (ratios of VIC times over fine grid times). With respect to the rigorous fine grid method, most of the reduction of CPU times is achieved with the brute force updates, further reductions with algorithms 1 and 2 are relatively small. This is because we applied to the fine grid the equivalent of algorithm 1 which reduces the CPU time (81.3 s versus 102.6). Inversely, with the approximate fine grid method, no reduction of CPU time

TABLE IV
REDUCTION FACTOR OF CPU TIME ACHIEVED WITH VIC FOR
THE PHANTOM HEAD

	v. s. rigorous fine grid	v. s. approximate fine grid
Brute force	8.62	5.75
Algorithm 1	9.45	7.27
Algorithm 2	9.80	7.53

TABLE V
MEMORY AND CPU TIME MEASUREMENTS FOR THE HUMAN BODIES

	Male Phantom	Female Phantom
Voxels	610x310x1840	530x300x1650
Total FDTD cells	353x203x968	313x198x873
CPU Time (min.)	46.2	35.4
Memory (GB)	30.3	23.0

Fig. 11. Observation of E_z within the skin and heart muscle of human phantoms.

is possible, so when using algorithms 1 or 2 with VIC, the difference with the brute force VIC is larger.

Finally, with the head phantom, the reduction of CPU time is smaller than with dielectric media [1], but it remains large, close to an order of magnitude, especially with the refinements of algorithms 1 or 2. This was also observed with the canonical Debye object in Section IV with which the reduction factors were higher than with the head phantom because the proportion of homogeneous VIC cells was larger.

Concerning the memory requirements, the VIC method needs storage of the three H components, the three E components in the two slices and at two time steps (12), and the three ΔD components in each voxel. For a number of VIC cells N_{vic}, this results in 39 N_{vic} real numbers. Similarly, for a number of fine grid cells $N_{fine} = 8 N_{vic}$, the rigorous fine grid method needs storage of 3 H, 6 E, 12 ΔD, in total 21 $N_{fine} = 168 N_{vic}$. For the approximate fine grid method, 12 $N_{fine} = 96 N_{vic}$. From this, the VIC method memory needs are reduced with factors about 4.3 and 2.4 with respect to the fine grid methods. In actual computations, additional arrays may be used to store coefficients of the update equations before the loop on time. Especially c_1, c_2, and c_3 in (12) for the 3 E components, in two slices, which need 18 N_{vic} memories, to be added to the 39 N_{vic} for storing the field components. Even with the additional storage of some other data, as the flags used with algorithms 1 and 2, the memory needs of the VIC method are always lower than those of a fine grid calculation, at least a factor of two with the rigorous one. As an example, with the head phantom, whose reduction of CPU times is given in Table IV, the memory needs were 1.1 GB with VIC, 3.1 GB with the rigorous fine grid, and 1.8 GB with the approximate fine grid.

VII. VIC-SIMULATIONS WITH WHOLE HUMAN BODY PHANTOMS

This section illustrates what can be done using the VIC method on a PC. We present the simulation results with two full-body phantoms. First, with the full body of the head phantom that we used in Section V, referred to as the "male phantom." Second, with the "female phantom" in [9]. The male phantom consists 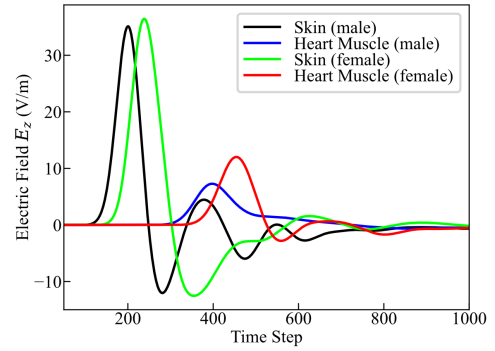of $610 \times 310 \times 1840$ voxels, while the female phantom is composed of $530 \times 300 \times 1650$ voxels, in both cases with a voxel size of 1 mm^3. The incident wave is the same as in Section V. Fig. 11 presents the simulation results at two locations, within the skin of the outer abdominal region, and the heart muscle. Note that the plotted E-fields significantly depend on the considered phantom, an influential parameter is probably the size.

The sizes of the FDTD domains of the VIC computations are presented in Table V. They include a 12 cell layer of vacuum surrounding the phantoms and a 12 cell PML. As can be seen, both the memory needs and the CPU times are compatible with the use of a PC, even without parallel computing. Using the same PC, the corresponding fine grid calculation would need a memory larger than 64 GB, which is usually not possible (most PCs are limited to 64 GB).

VIII. CONCLUSION

The VIC method presented in [1] in the case of pure dielectric objects has been extended to dispersive Debye media, in view of applications to bioelectromagnetics. Several experiments have shown that the accuracy and the limitations of the method are roughly similar to the ones observed with dielectric objects. The VIC method is by far more accurate than the averaging method, a significant error occurs only in the close vicinity of the singularities of the E-field, which is inherent to the larger size of the VIC cell. The limitations are obviously the same as in [1], mainly the upper-frequency cut-off which is lowered with the ratio of the VIC cell to the voxel size.

The reduction of the computational requirements is lesser than with dielectric objects, due to the complex constitutive relation of the Debye media, but it remains high, especially for the CPU time which is reduced by about one order of magnitude with VIC cells two times the voxels size. The VIC method is stable with Debye media, its stability condition remains the CFL condition of the FDTD method, as with dielectric media in [1]. Finally, the VIC method could also be applied to such other dispersive media as the Drude or Lorentz media using their own auxiliary equations in place of the Debye media one.

REFERENCES

[1] K. Tekbaş and J.-P. Bérenger, "Finite-difference time-domain (FDTD) method with non-homogeneous cells filled with voxels," *J. Comput. Phys.*, vol. 489, Sep. 2023, Art. no. 112266.

[2] E. Zastrow, S. K. Davis, M. Lazebnik, F. Kelcz, B. D. Van Veen, and S. C. Hagness, "Development of anatomically realistic numerical breast phantoms with accurate dielectric properties for modeling microwave interactions with the human breast," *IEEE Trans. Biomed. Eng.*, vol. 55, no. 12, pp. 2792–2800, Dec. 2008.

[3] Y. Zhao and Y. Hao, "Finite-difference time-domain study of guided modes in nano-plasmonic waveguides," *IEEE Trans. Antennas Propag.*, vol. 55, no. 11, pp. 3070–3077, Nov. 2007.

[4] A. Deinega and I. Valuev, "Subpixel smoothing for conductive and dispersive media in the finite-difference time-domain method," *Opt. Lett.*, vol. 32, no. 23, p. 3429, Dec. 2007.

[5] J. Liu, M. Brio, and J. V. Moloney, "Subpixel smoothing finite-difference time-domain method for material interface between dielectric and dispersive media," *Opt. Lett.*, vol. 37, no. 22, p. 4802, Nov. 2012.

[6] J. Hamm, F. Renn, and O. Hess, "Dispersive media subcell averaging in the FDTD method using corrective surface currents," *IEEE Trans. Antennas Propag.*, vol. 62, no. 2, pp. 832–838, Feb. 2014.

[7] K. Tekbas, F. Costen, J.-P. Bérenger, R. Himeno, and H. Yokota, "Subcell modeling of frequency-dependent thin layers in the FDTD method," *IEEE Trans. Antennas Propag.*, vol. 65, no. 1, pp. 278–286, Jan. 2017.

[8] K. Tekbas and J.-P. Bérenger, "FDTD algorithm for numerical anatomical models with cells containing several Debye media," *IEEE Trans. Electromagn. Compat.*, vol. 63, no. 3, pp. 947–950, Jun. 2021.

[9] A. Christ et al., "The virtual family—Development of surface-based anatomical models of two adults and two children for dosimetric simulations," *Phys. Med. Biol.*, vol. 55, no. 2, pp. N23–N38, Dec. 2009.

[10] (Jan. 2017). *The Media Parameters for the Debye Relaxation Model*. [Online]. Available: http://cfd-duo.riken.jp/cbms-mp/

Kenan Tekbaş (Member, IEEE) received the M.Sc. degree in communication engineering and the Ph.D. degree in electrical and electronic engineering from The University of Manchester, Manchester, U.K., in 2012 and 2017, respectively.

He is currently a Post-Doctoral Marie Skłodowska-Curie Fellow with the Department of Electromagnetism, University of Granada, Granada, Spain. His research interests include computational electromagnetics, the finite-difference time-domain method, numerical modeling of magnetic materials, bioelectromagnetism, and high-performance computing.

Jean-Pierre Bérenger (Fellow, IEEE) received the master's degree in physics from University Joseph Fourier, Grenoble, France, in 1973, and the master's degree in optical engineering from the Institut d'Optique Graduate School, Paris, France, in 1975.

From 1975 to 2013, he was with the French Ministry of Defense, where he held positions such as a Research Engineer, an Expert on the electromagnetic effects of nuclear bursts, and a Contract Manager. His technical works were mainly focused on numerical electromagnetics, including the finite-difference time-domain method, the absorbing boundary conditions, and the low-frequency propagation. From 2013 to 2023, he was a Visitor at the Department of Electrical and Electronic Engineering, the University of Manchester, U.K.

Mr. Bérenger received the 2014 John Howard Dellinger Gold Medal from URSI. He was an Associate Editor for IEEE TRANSACTIONS ON ANTENNAS AND PROPAGATION from 2006 to 2010.

Luis Manuel Diaz Angulo (Member, IEEE) received the M.Sc. and Ph.D. degrees in physics and the M.Sc. degree in electronics engineering from the University of Granada, Granada, Spain, in 2008, 2014, and 2015, respectively.

He is currently an Associate Professor with the Department of Electromagnetism and State Matter, University of Granada. He has worked in time-domain computational electromagnetics, especially discontinuous Galerkin and finite differences. His research interests include electromagnetic compatibility and material characterization.

Miguel Ruiz-Cabello was born in Granada, Spain. He received the B.Sc. and M.Sc. degrees in physics and the Ph.D. degree from the University of Granada, Granada, in 2008, 2010, and 2017, respectively.

His current research interests include computational electrodynamics in the time domain, especially the finite-differences time-domain (FDTD) method, subgridding, conformal techniques, high-performance computing, radar cross section, and parameter retrieval.

Salvador G. Garcia (Senior Member, IEEE) received the M.Sc. and Ph.D. degrees (Hons.) in physics from the University of Granada, Granada, Spain, in 1989 and 1994, respectively.

He is a Full Professor with the Department of Electromagnetism and Matter Physics, University of Granada. In 2010, he co-founded the startup Elemwave devoted to numerical solver development and EM consultancy. He has published over 90 refereed journal articles and book chapters and led several national and international projects. His current research interests include computational electromagnetics, electromagnetic compatibility, RCS, antenna design, and material analysis.